Development of an antibody panel for imaging mass cytometry to investigate cancer-associated fibroblast heterogeneity and spatial distribution in archival tissues

Stian Tornaas*[1], Dimitrios Kleftogiannis[1,3], Siren Fromreide[1], Hilde Ytre-Hauge Smeland[1,2], Hans Jørgen Aarstad[4], Olav Karsten Vintermyr[2], Lars A. Akslen[1,2], Daniela Elena Costea[1,2], Harsh Dongre[#1,2]

[1]Center for Cancer Biomarkers CCBIO and Gade Laboratory for Pathology, University of Bergen, Norway

[2]Department of Pathology, Haukeland University Hospital, Bergen, Norway

[3]Computional Biology Unit, Department of Informatics, University of Bergen, Norway

[4]Department for Ear-Nose-and-Throat, Head and Neck Clinic, Haukeland University Hospital, Bergen, Norway

*** Correspondence:**
Corresponding author
*stian.tornaas@uib.no

#harsh.dongre@uib.no

Keywords: cancer associated fibroblasts, heterogeneity, imaging mass cytometry, immunohistochemistry, bioinformatics.

Abstract

Introduction: Cancer associated fibroblast (CAF) mediated crosstalk with other tumor compartments is shown to modulate cancer development and progression. Conventionally, CAFs are known to promote tumorigenesis either by secreting a wide range of growth factors, cytokines, and chemokines or by remodeling the underlying stroma. However, recent studies aimed at depleting CAFs have shown progression to more aggressive tumors leading to poorer outcomes. This may be attributed to the heterogeneity and plasticity of CAFs. Understanding CAF heterogeneity has been limited due to the lack of specific markers. Imaging mass cytometry (IMC) can analyze up to 40 parameters at subcellular resolution simultaneously and hence it can be an ideal tool to unravel the heterogeneity of CAFs and decipher the role of various CAF subsets in cancer development and progression. The aim of this study was to develop a panel of antibodies (ABs) for IMC to identify different CAF phenotypes and their spatial distribution in tissues and other tumor components in formalin-fixed paraffin-embedded (FFPE) archival tissues.

Methods: A comprehensive panel of ABs were chosen based on known literature on CAFs and other tumor and microenvironment-related markers. ABs were conjugated to rare earth metals using the protocol provided by the supplier (Fluidigm, CA, USA). FFPE tissue samples from different organs/lesions known to express certain markers were used for making control tissue microarrays (cTMAs) for verification of conjugated ABs. Immunohistochemistry (IHC) with metal-conjugated ABs was used as the “gold standard” for optimization of IMC. Tissue images were segmented using ImcSegmentationPipeline (Ilastik and CellProfiler). Downstream analysis of single-cell data was

performed using a newly developed bioinformatics pipeline as well as ImaCytE, an existing software solution.

Results: The final panel of ABs was decided based on a comparable performance of conjugated ABs validated using IHC and IMC. Different cell types were identified including various subsets of CAFs and immune cells using cell segmentation and unsupervised clustering.

Conclusion: This study establishes an extensive panel of IMC ABs on archival FFPE tissue material for unravelling CAF heterogeneity. In addition, the panel described here, the downstream analysis and the newly developed pipeline can be readily applied to different tissue types in context of cancer research or other fibrotic disease.

1 Introduction

Development and progression of cancer is a complex process governed not only by cancer cells but also supported by many types of surrounding non-transformed cells. These surrounding cells include fibroblasts, mesenchymal cells, pericytes, cells related to blood and vascular system, fat, and nerve cells, as well as immune cells such as T and B cells, natural killer (NK) cells, myeloid-derived suppressor cells and macrophages (1). These cells, along with soluble growth factors and extracellular matrix (ECM), comprise the tumor microenvironment (TME) (2). Fibroblasts within the TME are known as cancer associated fibroblasts (CAFs) and they represent a heterogenous population of cells that have either anti- or pro-tumorigenic functions (3-5). These functions involve support of tumor cell proliferation and migration, angiogenesis, immunomodulation and chemoresistance exerted by secretion of different growth factors, chemokines, cytokines or by their own motile phenotype (6-9). Due to the long-held notion that CAFs support tumor progression, attempts have been made to deplete CAFs in tumors, albeit with poor outcomes (10). This might demonstrate CAF heterogeneity and reflect the high plasticity of CAFs attributed to their multiple origins and functions. To date, there is no consensus for markers of CAFs, and the majority of studies define CAFs by a combination of spatial location, morphology and lack of expression of linage markers for epithelial cells, leukocytes and endothelial cells (11).

Imaging mass cytometry (IMC, Hyperion™) is a relatively new technology that allows multiparametric analysis and gives spatial overview of different cell types and molecules in formalin-fixed paraffin embedded (FFPE) tissue (12). In principle, the technology resembles immunohistochemistry (IHC) because the basic steps involved are similar (antigen retrieval and antigen-antibody reaction). However, the visualization of the antigen-antibody reaction is different: while presence of antigens in samples processed by IHC is visualized by a chemical reaction and observed through a light microscope, IMC produces a digitalized reconstruction of tissue based on the presence of ABs conjugated to rare earth metals of the lanthanide series (13). A laser ablates the tissue from the region of interest (ROI) pulse-wise, and each time the laser hits the tissue, it liberates the metals that are bound to ABs in that particular area (or pixel) which produces a plume of metals. Since each AB/marker has been designated with a particular metal with different masses/weight, the machine can distinguish the different markers based on time-of-flight for each metal (14). Because of this, the technology enables *in situ* characterization of tissue samples and can help unravel the complexity of TME.

The IMC technology has been used to increase our understanding of several types of cancer (13, 15). Nevertheless, the use of this advanced technology requires thorough validation of markers for

optimal performance of the Hyperion system. The aim of this study was to develop a panel of ABs that could be used to distinguish different CAF subsets based on variation in marker expression and how these phenotypes organize themselves in tissue in addition to tumor- and immune cells and structures related to vasculature. We have previously reported the possibility to distinguish at least two subsets of CAFs in head and neck squamous cell carcinoma by transcriptomic studies on isolated primary CAFs in culture. In these studies, integrin α11 demonstrated to be a central protein/biomarker for CAF phenotypes (16, 17). We describe here the development of a panel consisting of 24 markers that can be used with IMC to stain human FFPE tissue sections. In addition, the panel includes conventional CAF markers for understanding their heterogeneity. These markers were selected based on previous knowledge of markers involved in cancer cell proliferation, migration, invasion, and metastasis, in addition to CAF subtypes and immune-related markers (18-22). To the best of our knowledge, this panel of markers have not been used with IMC before and can give additional insight to CAFs` function and role in cancer. The panel established in this study comprises epithelial and structural markers, markers for immune (NK cells, macrophages, T helper cells, cytotoxic T cells, T-regulatory cells, and B cells) and vascular (blood & lymph endothelial cells and pericytes) cells. The work described here establishes a powerful IMC protocol to decipher CAF heterogeneity and identify key actors in tumor development and resistance to therapies. The AB panel could be applied across various types of cancer and other pathological processes such as fibrosis to increase our knowledge about CAFs. The main steps and optimization strategy used here can also serve as basis for developing panels for investigating other types of cells/pathways both in cancer and in other pathologies/normal tissues.

2 Materials and methods

Patient material

To standardize the protocol, “control” tissue micro arrays (cTMAs) were made from archival FFPE blocks. The FFPE blocks were obtained from 35 patients undergoing treatment at the Haukeland University Hospital, Bergen, Norway. Patient samples were anonymized, and all patient informed consents were collected according to the Declaration of Helsinki (REK 2010/481;2011/125). The cTMA samples used as positive controls are listed in Supplementary Table S1. These tissues were chosen based on previously documented (by their respective suppliers) positive expression of the various markers included in our panel. From the cTMA block, four µm-thin tissue sections were cut and placed on glass slides (Thermo Scientific, J1800AMNZ, MA, USA) and subsequent staining was performed.

Antibodies and metal conjugation

Designing a multiparametric AB panel for IMC studies relies on quality of rare-earth metals (or isotopes) and conjugating them with appropriate ABs. Usually, the most optimal metals are in the atomic mass range of 159 – 170 kDa (Fluidigm, CA, USA), and therefore, these should be conjugated to low-abundance antigens and vice-versa for high-abundance antigens to less optimal metals. When metal-AB combination was decided, Panel designer, an online program developed by Fluidigm to evaluate spill-over between channels was used for optimizing AB panel. Carrier-free ABs were conjugated to metals in the lanthanide series of chemical elements with various epitopes using MaxPar conjugation kits (Fluidigm, South Francisco, CA, USA) using suppliers` protocol (Table 1). Briefly, conjugation started with incubation of polymers together with metals and simultaneous washing of ABs in two separate procedures. When polymer was attached to metal and AB was properly reduced in separate microtubes, both were mixed and incubated at 37ºc for 90 min.

Afterwards, conjugated antibodies (cABs) were first tested with IHC to determine optimal concentration and incubation using cTMAs. Then, cABs were validated with cTMAs and IMC which was then compared with results from IHC to determine their performance (specificity and affinity).

Immunohistochemistry

ABs for IMC were first tested with conventional IHC both before and after metal conjugation to validate each ABs staining quality. Sections were baked over night at 60ºc and deparaffinized with xylene and decreasing concentration of alcohol. Antigen retrieval was done at pH9 (Dako, S2367, CA, USA) using a pressure boiler (BioCare Medical Model DC2008INTL, CA, USA) at 120ºc for 10 min. Endogenous peroxidase activity was blocked with 3 % hydrogen peroxidase solution (Dako, S2023, CA, USA) for 5 min. Further, samples were washed with tris buffered saline with tween (TBST) for 10 min before unspecific protein binding was blocked with 10 % goat serum (Dako, X0907, CA, USA) in 3 % bovine serum albumin (BSA) (Merck, A3059, Darmstadt, Germany) for 20 min. Slides were then subjected to primary AB for 60 min at room temperature (RT) or overnight at 4ºc (Table 1). After washing with TBST twice for 5 min each, slides were incubated with secondary horseradish peroxidase (HRP) conjugated (Dako, K8000, CA, USA) AB for 30 min. AB binding was visualized with chromogen diaminobenzidine (DAB) (Dako, K8012, CA, USA) for 10 min. Slides were then counterstained with hematoxylin (Dako, S3301, CA, USA) and dehydrated by increasing concentration of alcohol and xylene before mounting with cover glass using pertex (HistoLab, 00811-EX, Askim, Sweden). Slides were scanned using Hammamatsu whole slide digital scanner (Company) and visualized using NDP.view2 plus v2.9.25.

Protocol for IMC staining

Tissue sections were deparaffinized by baking the slides overnight at 60 ºc. The next day, slides were dewaxed in fresh xylene twice for 10 min each followed by rehydration in descending grades of fresh alcohol (100 %, 95 %, 70 %) for 5 min in each grade. Slides were then washed in MilliQ water for 5 min before antigen retrieval was done with pressure cooker at 120ºc for 10 min. Samples were then cooled down until 70ºc and washed with MilliQ water for 10 min and then 10 min with “homemade” PBS. Hydrophobic barrier was drawn followed by blocking with 3 % BSA in MaxPar PBS (Fluidigm, CA, USA) for 45 min at room temperature in a humid chamber. The blocking solution was shaken off and overnight AB mix was applied and incubated overnight at 4ºc. The next day, slides were washed with MaxPar PBS supplemented with 0.2 % Triton X100 (Merck, Darmstadt, Germany) thrice for 5 min each and then applying next round of AB mix, which were incubated for 1 hour at room temperature. Slides were washed again with Maxpar PBS with 0.2 % Triton X100 thrice for 5 min each followed by incubation with Ir solution for 5 min. Slides were washed trice with MaxPar PBS 5 min each and then briefly with MilliQ before drying the sections.

Acquisition of data with Imaging mass cytometry (IMC)

Images were acquired using Hyperion imaging system (Fluidigm) and the system was tuned according to manufacturer`s protocol. Regions of interest were selected from cTMA cores, and the areas were laser-ablated at 200 Hz which produces pixel size/resolution of 1 μm^2. The energy needed to obtain adequate ablation of tissue varies between tissue types. Therefore, a small part of ROI from each tissue type was selected to observe if energy level was satisfactory or not and adjusted according to best performance. Either energy level 0 or 1 was used for TMA cores in study. The following preprocessing of raw data was done using commercially available acquisition software CyTOF software v7.0 (Fluidigm), and visualization was done using MCD Viewer v1.0.560.6

(Fluidigm). The MCD viewer was then used to confirm the ROI success and produce high-quality images with selected combination of markers.

Image processing and cell segmentation

Segmentation of raw IMC data was done using a combination of Ilastik (23) and CellProfiler (24) following the "gold standard" pipeline ImcSegmentationPipeline (25). Briefly, raw data from MCD files were extracted in TIFF format using a graphical interface provided by the Anaconda Navigator v3. Two different image stacks were made from each ROI namely: oral squamous cell carcinoma (OSCC), tonsil, placenta, and osteosarcoma. "Full" stack contains all channels chosen to be used for the analysis, while the "Ilastik" stack contains channels chosen to be used for pixel classification and cell segmentation.

During the cell segmentation step, individual cells and regions of tumor and stroma were segmented to generate probability map by classifying pixels to three classes namely: nucleus, cytoplasm/membrane, and background. A combination of AB stains from the "Ilastik" stacks was used to identify membranes and nuclei. Single-cell segmentation masks and TIFF images of the AB channels were overlaid and the mean expression levels of markers and spatial features of single-cells as well as the direct neighbors of each cell were identified and exported to csv format using the HistoCAT software (26).

The data presented in this study were not transformed, and the raw AB intensities were used for further downstream analyses. To the best of our knowledge, there is no consensus strategy about the transformation of IMC data, and therefore different studies have applied different transformation techniques (15, 27, 28). The single cell data were censored at the 99th percentile to remove outliers, and z-scores were produced for visualization in t-SNE (full form?) plots and heatmaps.

Downstream analysis

Single cells from different samples were clustered into groups of phenotypical similar cells based on an unsupervised clustering approach. Initially the FlowSOM algorithm (29) was used to generate 225 (grid of 15x15) group of cells. For high-dimensional clustering of single-cells, 24 markers were used namely: α-SMA, caveolin-1, collagen-1, CD4, CD8a, CD16, CD20, CD31, CD68, CD90/Thy-1, CD140β, CD146, CD163, E-cadherin, EGFR, FAP, FoxP3, FSP-1/S100A4, integrin α-11, Ki-67, podoplanin, tenascin-C, VEGFR-2, and YAP-1. The resulting 225 clusters were aggregated based on the ConsensusClustering method (30) with Euclidean distance metric and average linkage. To assess the quality of each aggregated meta-clustering solution, the Proportion of Ambiguous Clustering (PAC) metric was estimated (31). To maintain relatively low-level ambiguity, and in order to detect rare groups of phenotypically similar cells, we merged meta-clusters at a PAC cutoff of 1%. At this PAC level, meta-clusters that showed a marker expression typical of endothelial, immune, and epithelial cells were aggregated together. The remaining cells were grouped together and annotated using known combinations of CAF-related markers, resulting in six CAF subgroups. One additional phenotypic subgroup was included to annotate all other single cells that exhibited "non-standard" marker expression profiles. We note here that the resolution and the detail at which groups of phenotypically similar cells are clustered together depends strongly on the AB panel, the tissues of interest, and the focus of the studied cell types. Here, since the focus is to investigate CAF heterogeneity, we do not provide a fine-grained distinction of immune, endothelial, stromal, or epithelial cell types. Moreover, since the field of annotating single-cells from CyTOF and IMC is

well-studied, there are additional unsupervised, semi-supervised and machine learning-based methods that are equally applicable for effective phenotypic annotation of single-cells (32-34).

For visualization of high-dimensional single-cell data into the 2D space we utilized the t-SNE (35) dimensional reduction algorithm. We used as input the full set of 24 markers, and the algorithm was run with default parameters (perplexity = 30, theta = 0.5) on the full set of cells (n=21,721).

Development of bioinformatics analysis workflow and code availability

The single cell analysis workflow described here was implemented in R, and the codes are publicly available at https://github.com/dkleftogi/IMC_DataAnalysis. The workflow allows users to extract single-cell data information from segmented IMC images, cluster phenotypical similar cells, perform basic exploratory data analysis and visualization of single-cells using heatmaps and t-SNE plots. To investigate the spatial location single-cells, and visualize the tissue structures we adopted functionalities from Cytomapper package (36), and we provide tissue visualization routines.

For users with limited programming knowledge, similar downstream analysis workflow can be performed using the ImaCytE software (37). ImaCytE offers a graphical interface that allows for cellular phenotypical annotation via unsupervised clustering, visualization via t-SNE and functions for single cell data localization and inspection.

Multiplex data analysis

3 Results

Establishment of a robust antibody panel

To develop a robust panel for investigating CAF heterogeneity using IMC, several (>40) markers were tested (Table 1). Different clones of ABs were selected based on available literature and in-house knowledge with a particular focus on CAF markers. Some of the ABs were excluded after the first validation on classical IHC using the same protocol for all ABs, as described in materials and methods. The twenty-eight ABs that performed well were taken further. In addition to fifteen available metal-conjugated ABs, thirteen more ABs were conjugated in-house. All markers included in the study underwent extensive quality check with the performance assessed by IHC both before and after conjugation. Moreover, all ABs included in the study underwent protocol standardization using different primary AB incubation times and temperatures (1hour and overnight at 4ºc).

After metal conjugation, low signal/background ratio was obtained with IMC for the ABs against NG-2 and VE-cadherin despite use of several adjustments to the protocol, suggesting conformation changes or destruction of antigen binding sites of these ABs (Supplementary Figure S1). From the rest, eleven in-house conjugated markers and thirteen pre-conjugated markers worked with high pH (pH9) antigen retrieval buffer in IHC. AB performance- (high signal and low background) was then evaluated with different primary AB incubation time in IHC. For example: better signal to noise ratio was observed in CD140β staining when incubated overnight as compared to 1hour at RT (data not shown). When compared to IHC, most of the ABs revealed comparable staining patterns in IMC, although the staining intensity was different (Figures 1, 2, 3). This can be attributed either to multiplexing of various ABs in IMC leading to spatial competition of AB binding or lack of signal amplification step in IMC. In contrast, antibodies against arginase-1, granzyme B and PD-L1, pFAK

and pTAK were excluded as satisfactory results regarding specificity and signal-to-noise ratio were not obtained even after trying different concentration, antigen retrieval buffers and incubation times (Supplementary Figure S1).

Discovery of single cell spatial localization and cell segmentation across tissue types

Visual inspection of staining was first done with MCD viewer. AB panel described in this study focused on structural markers (OSCC core from cTMA, Figure 1), CAF heterogeneity (osteosarcoma core from cTMA, Figure 2) and immune cell subsets (tonsil core from cTMA, Figure 3). To begin with, an OSCC tissue core from the cTMA containing structural and vascular compartments was chosen to validate the markers: E-cadherin, collagen-1, tenascin-C, CD31 and podoplanin. These were further used to visualize cells related to epithelial, stromal, and vascular tumor compartments respectively (Figure 1). E-cadherin was restricted to the epithelial compartment whereas collagen-1 and tenascin-C revealed the stromal compartment of the tumor as observed by both IMC and IHC (Figure 1). In addition, majority of cancer cells showed EGFR expression, whereas Ki-67 depicted proliferating cells in both the cancer and stromal compartment (Supplementary Figure S2). Osteosarcoma tissue core from the cTMA was chosen to validate the presence of the more classically accepted CAF markers: α-SMA, integrin α11, FAP, collagen-1, FSP-1, CD140β, caveolin-1 and CD90 (Figure 2 and Supplementary Figure 3). α-SMA and FAP were observed to be expressed by one subset of cancer cells and integrin α11 and collagen-1 by another (Figure 2), by both IMC and IHC. Similarly comparable staining of FSP-1, CD140β and caveolin-1 was observed between IMC and IHC in the osteosarcoma core of the cTMA (Supplementary Figure S3). In the tonsil cTMA core, various immune cell types were identified – in a similar way by both IMC and IHC: $CD4^+$ (T helper cells), $CD8^+$ (cytotoxic T cells), $CD20^+$ (B cells), $CD4^+$ $FoxP3^+$ (T regulatory cells) and $CD68^+$ (macrophages) (Figure 3). Moreover, $CD16^+$ (natural killer cells) and $CD163^+$ (M2 macrophages) could be detected in the OSCC core of the cTMA (Supplementary Figure 4). The frequencies of Foxp3+, CD20+, CD4+, CD68+, CD163+, CD8+ and Ki67+ cells determined by IMC were comparable with the matched pathological IHC scores (Supplementary Figure S4).

Two-dimensional graphs using the dimensionality reduction algorithm t-distributed stochastic neighbor embedding (t-SNE) were generated to visualize cells from different samples and cell types in each sample (Figure 4A, B). t-SNE plots confirmed presence of different cell lineages with a majority of cells from tonsil expressing various immune markers, osteosarcoma expressing mesenchymal markers and placenta expressing both structural and vascular compartments (Supplementary Figure S5A). Interestingly, placenta-specific and osteosarcoma-specific clusters separated from both OSCC and tonsil clusters as well as from each other. Although, an OSCC-dominant cluster could be seen containing mainly epithelial markers, the cells were spread across all the samples, suggesting presence of different cell lineages in OSCC tumor. Upon cell segmentation, a total of 21,721 cells from all four cTMA cores could be identified, with tonsil having 9826 segmented cells (45.3%), followed by OSCC (33.7 %), osteosarcoma (10.7 %) and placenta (10.3 %) (Supplementary Figure 5B). Combined from all four cTMA, 44.2% were immune cells, 27.7% were cancer cells/epithelial cells, 4.8% were endothelial cells, 9.2% remained unassigned (low expression of all markers) and the rest (14.1%) were defined as stromal cells (https://github.com/StiThor/Development-of-antibody-panel-for-imaging-mass-cytometry-to-investigate-cancer-associated-fibroblast) (Figure 4C, D). We next classified the stromal cells (3061 cells) into different CAF metaclusters based on PAC cut-off and previous knowledge of CAF markers (Supplementary figure S5C, D). In total, the stromal cells clustered into six different subsets, with all except CAF-4 subset present in osteosarcoma. OSCC cTMA had a majority of CAF-4 subset, followed by CAF-5 and CAF-6. In addition, clustering revealed the expression of different CAF

markers in the six CAF subsets (Figure 4e). Previously defined CAF subsets could be identified as: cluster 1, CAF-1- α-SMA^{high}, CAV-1^{med}, CD140β^{high}, FAP^{high}, ITGA11^{neg}, Col-1^{high}, FSP1^{neg}, CD90^{high}; CAF-2- α-SMA^{low}, CAV-1^{low}, CD140β^{high}, FAP^{high}, ITGA11^{neg}, Col-1^{high}, FSP1^{neg}, CD90^{high}, CAF-6- α-SMA^{high}, CAV-1^{high}, CD140β^{neg}, FAP^{neg}, ITGA11^{high}, Col-1^{low}, FSP1^{neg}, CD90^{low} and CAF-3- α-SMA^{low}, CAV-1^{low}, CD140β^{med}, FAP^{med}, ITGA11^{neg}, Col-1^{high}, FSP1^{neg}, CD90^{med} (Figure 4e) (38). In addition to previously identified CAF subsets, two more subset defined by expression of collagen-1 and CD90 could be observed (Figure 4e): CAF-5- α-SMA^{neg}, CAV-1^{neg}, CD140β^{neg}, FAP^{neg}, ITGA11^{neg}, Col-1^{high}, FSP1^{neg}, CD90^{neg} ; and CAF-4- α-SMA^{low}, CAV-1^{neg}, CD140β^{neg}, FAP^{neg}, ITGA11^{low}, Col-1^{low}, FSP1^{neg}, CD90^{med}. Abundance-wise, CAF-3 subset was highest in number (1091 cells, 5.02%) and mostly present in the osteosarcoma cTMA. The next-most abundant subset was CAF-5 with highest expression of collagen-1, present in both osteosarcoma and OSCC. Collagen-1 overexpressing CAFs were previously shown to have a tumor restraining function by mechanically restraining metastasis to liver in pancreatic and colorectal cancers (39). Interestingly, visualization of these cells in OSCC tissue showed closer proximity to cancer cells (Figure 5A). It would be of major interest to identify these subsets in a cohort of OSCC cases and investigate if the abundance of different CAF subsets in the stroma of OSCC correlate with clinical parameters including survival. In addition to this, expression of all 24 markers in different metaclusters is shown in Supplementary Figure S6.

Similar downstream analysis workflow was preformed using the ImaCytE software (37). Cellular phenotypical annotation via unsupervised clustering and subsequent visualization via t-SNE revealed three different CAF metaclusters (Figure 5B, C). These clusters were similar to CAF-1, CAF-6 and CAF-4 (Figure 5C). Taken together, these results suggest that the IMC panel is robust, and the analysis pipeline provides adequate cell segmentation with immense potential for further applications.

4 Discussion

We describe here a panel consisting of 24 ABs focusing on deciphering CAF heterogeneity in FFPE tumor tissues using imaging mass cytometry (Hyperion). Hyperion technology utilizes CyTOF (cytometry time-of-flight) to detect different metals based on their molecular weight and thereby separating various epitopes/targets. Both FFPE and frozen tissue can be used with the system, which provides a huge advantage, since many laboratories have access to archival tissue that forms the basis of large cohorts-based retrospective studies. The method of IHC is widely used in biomarker discovery, and as a diagnostic tool in clinical practice (40, 41). However, there is a limitation to IHC regarding the number of ABs that can be used simultaneously and thereby limiting the information obtained. Cancer as a disease, is daunting in its breadth and heterogeneity due to genetics, differences in cell and tissue biology, response to therapy and pathology. More powerful experimental and technical tools are required to provide a “snapshot” of the tumor along with its microenvironment. IMC is one such technique that has the possibility to use up to 121 different channels and by that in principle 121 different ABs (42). However, currently it is not possible to use more than 40 different ABs due to limits regarding available metal isotopes (43, 44). Nonetheless, this is a huge improvement on simultaneous detection of protein expression in tissues as compared to IHC and is able to capture the vast complexities of tumor and its microenvironment. In future, wider use of IMC will give a broader repertoire of ABs that can be implemented in Hyperion panels, as well as a better understanding to conjugate metals for producing best results.

Conventional “big data” obtained from IMC requires a complex workflow. A typical IMC workflow includes image acquisition, single cell segmentation, single cell data transformation/normalization and phenotypic annotation of single cells typically via unsupervised clustering (45). After image acquisition, single cell segmentation (ImcSegmentationPipeline) with Anaconda/Jupyter developed by Jackson et al (27) was used in this study. Segmentation of cells using Anaconda/Jupyter is a fairly straight forward process where markers are selected to be used for nuclear and cytoplasm pixel classification that will later on establish what will define the different cell compartments (25, 46). A common method for analyzing IMC data is by using Histology Topography Cytometry Analysis Toolbox (HistoCAT). This is a program that makes it possible to cluster cells based on marker expression, obtaining single-cell information and discover cell neighborhoods, but the program has a significant drawback. It does not allow spatial visualization of cells in tissues and does not scale well as the image volume increases (26, 47). This could be circumvented by different software utilities implemented in one of the prevalent programing languages in bioinformatics, such as Python or R (48). Here, we developed and share with open-source license, a basic IMC data analysis workflow that can be used in subsequent studies. We also recommend an interactive visual analysis workflow called ImaCytE. The latter is quite similar to HistoCAT, and offers user friendly utilities for single-data exploration, visualization and clustering of cells (37).

A better understanding of tumor microenvironment (TME) is imperative for identifying clinically relevant single-cell signatures for improved patient care. CAFs in TME play a dual role, they are shown to enhance tumor cell proliferation, invasion and metastasis but also prevent cancer cell invasion (21). This dual role has been explained by variety of markers used to define CAFs and lack of a general definition (11). In addition, CAFs are known to mediate response to immune checkpoint inhibitors (ICI) therapy (49) and hence it is pertinent to decipher the heterogeneity to identify therapeutic targets for future combinatorial trials. Our IMC panel represents a comprehensive set of targets for spatial characterization of CAFs and its interactions with immune cells and other TME components. It includes eleven markers that have not been reported in IMC yet and sheds light on novel perspectives.

Our panel and subsequent downstream analysis paradigm could aptly differentiate between different tumor compartments. The cTMA cores presented in detail in this study were chosen as such to have majority of one compartment: OSCC as structural component, osteosarcoma for stromal component, placenta for vascular component, and tonsil for its immune-related component. Eight distinct CAF markers α-SMA, collagen-1, CAV-1, CD140β, FAP, integrin α11, FSP-1 and CD90 were used to comprehensively study CAF subsets. All markers were used to generate clusters of cells across tissue types. CAF-1 cluster α-SMA^{high}, CAV-1^{med}, CD140β^{high}, FAP^{high} and CD90^{high} was mostly detected in osteosarcoma as well as in OSCC but not in either placenta or tonsil. Similarly, the same pattern of expression in osteosarcoma and OSCC was observed with CAF-2 cluster with α-SMA^{low}, CAV-1^{low}, CD140β^{high}, FAP^{high} and CD90^{high}. On the other hand, a cluster of CAFs with caveolin-1^{high} and integrin α11^{high} (CAF-6) was found in the stromal part of all four tissues in focus, with the most abundant being in OSCC. Importantly, we also found a subset of CAFs with collagen-1 overexpression, which has been shown to have a protective role by mechanical restriction to liver metastasis of pancreatic and colorectal cancer (39). This opens new avenues to quantify CAF subsets with restrictive role against more tumor promoting subsets in larger cancer cohorts. The IMC panel described here will in the future be used to validate such findings. The result also demonstrated that OSCC contained different immune subtypes, although lower in number of cells compared to tonsil. Of note, the presence of immune cells in osteosarcoma and placenta was negative/low.

IMC technology faces several challenges before widespread adoption. Suitable ABs that are provided in a carrier-free/MaxPar ready format for conjugation to metals must be validated both before and after conjugation. Metal conjugation may change the antigen binding site and hence might affect performance of ABs. In addition, fine-tuning of both staining/incubation of ABs and machine for obtaining low background/high specificity is needed. A key requirement for designing and choosing an AB panel for IMC experiments is that all ABs must work with the same antigen retrieval protocol. Finally, it also must be kept in mind that highly multiplex AB reaction might affect the performance due to the spatial distribution of antigens. During the analysis of AB expression values, attention must be paid to the problem of channel crosstalk. However, well designed AB panels, similar to the one presented here, are minimally affected by channel spillover. In the near future, we are planning to incorporate the CATALYST R package in our downstream analysis workflow. We are also conducting research related to the normalization and transformation strategies of AB expression values to select the most appropriate ones for future projects. In addition to fully utilize the spatial information of single-cells, we are planning to implement neighborhood analysis utilities and investigate properties of single-cell communities using standards network analysis methods.

Despite assiduous research, the role of CAFs in tumor initiation, progression and resistance to therapy is still mystery (50). Unveiling the secrets behind CAF heterogeneity and the functions of various subclasses might improve medicine aiming to deplete CAFs that are pro-tumorigenic and boost CAFs that are anti-tumorigenic. To our understanding, there are no established IMC panels having focus on CAF heterogeneity and, therefore, this work will support the future work of understanding these cell types.

5 Conflict of Interest

The authors declare that the research was conducted in the absence of any commercial or financial relationships that could be construed as a potential conflict of interest.

6 Author Contributions

Conceptualization, ST., DK., DEC. and HD.; data curation, ST, DK and HD.; formal analysis, ST , DK and HD.; funding acquisition, LA, OKV, HJA and DEC.; investigation, ST, DK, SF, HYHS, DEC and HD.; methodology, ST, DK, SF, HYHS, HJA, OKV, LA, DEC and HD.; project administration, DEC and HD.; supervision, DK, LA, DEC and HD.; validation, DK, ST, SF and HD.; visualization, ST, DK and HD.; writing—original draft, ST.; writing—review & editing, ST, DK, SF, HYHS, HJA, OKV, LA, DEC and HD. All authors have read and agreed to the published version of the manuscript.

7 Funding

This work was supported by the Research Council of Norway through its Centers of Excellence funding scheme, (Grant No. 22325), The Western Norway Regional Health Authority (Helse Vest Grant No. 912260/2019) and The Norwegian Centre for International Cooperation in Education (project number CPEA-LT-2016/10106).

8 Acknowledgments

This is a short text to acknowledge the contributions of specific colleagues, institutions, or agencies that aided the efforts of the authors.

9 References

1. Mao X, Xu J, Wang W, Liang C, Hua J, Liu J, et al. Crosstalk between cancer-associated fibroblasts and immune cells in the tumor microenvironment: new findings and future perspectives. Molecular Cancer. 2021;20(1):131.

2. Roma-Rodrigues C, Mendes R, Baptista PV, Fernandes AR. Targeting Tumor Microenvironment for Cancer Therapy. Int J Mol Sci. 2019;20(4):840.

3. Chen X, Song E. Turning foes to friends: targeting cancer-associated fibroblasts. Nature Reviews Drug Discovery. 2019;18(2):99-115.

4. Ping Q, Yan R, Cheng X, Wang W, Zhong Y, Hou Z, et al. Cancer-associated fibroblasts: overview, progress, challenges, and directions. Cancer Gene Therapy. 2021;28(9):984-99.

5. Kalluri R. The biology and function of fibroblasts in cancer. Nature Reviews Cancer. 2016;16(9):582-98.

6. Louault K, Li R-R, DeClerck YA. Cancer-Associated Fibroblasts: Understanding Their Heterogeneity. Cancers (Basel). 2020;12(11):3108.

7. Chen Y, McAndrews KM, Kalluri R. Clinical and therapeutic relevance of cancer-associated fibroblasts. Nature Reviews Clinical Oncology. 2021;18(12):792-804.

8. Tao L, Huang G, Song H, Chen Y, Chen L. Cancer associated fibroblasts: An essential role in the tumor microenvironment. Oncol Lett. 2017;14(3):2611-20.

9. Valkenburg KC, de Groot AE, Pienta KJ. Targeting the tumour stroma to improve cancer therapy. Nat Rev Clin Oncol. 2018;15(6):366-81.

10. Özdemir BC, Pentcheva-Hoang T, Carstens JL, Zheng X, Wu C-C, Simpson TR, et al. Depletion of carcinoma-associated fibroblasts and fibrosis induces immunosuppression and accelerates pancreas cancer with reduced survival. Cancer Cell. 2014;25(6):719-34.

11. Sahai E, Astsaturov I, Cukierman E, DeNardo DG, Egeblad M, Evans RM, et al. A framework for advancing our understanding of cancer-associated fibroblasts. Nature Reviews Cancer. 2020;20(3):174-86.

12. Naderi-Azad S, Croitoru D, Khalili S, Eder L, Piguet V. Research Techniques Made Simple: Experimental Methodology for Imaging Mass Cytometry. Journal of Investigative Dermatology. 2021;141(3):467-73.e1.

13. Ijsselsteijn ME, van der Breggen R, Farina Sarasqueta A, Koning F, de Miranda NFCC. A 40-Marker Panel for High Dimensional Characterization of Cancer Immune Microenvironments by Imaging Mass Cytometry. Frontiers in Immunology. 2019;10(2534).

14. Chang Q, Ornatsky OI, Siddiqui I, Loboda A, Baranov VI, Hedley DW. Imaging Mass Cytometry. Cytometry Part A. 2017;91(2):160-9.

15. Ali HR, Jackson HW, Zanotelli VRT, Danenberg E, Fischer JR, Bardwell H, et al. Imaging mass cytometry and multiplatform genomics define the phenogenomic landscape of breast cancer. Nature Cancer. 2020;1(2):163-75.

16. Eble JA, Gullberg D. What Is the Fuss about Integrins and the Tumor Microenvironment? Cancers (Basel). 2019;11(9):1296.

17. Zeltz C, Alam J, Liu H, Erusappan PM, Hoschuetzky H, Molven A, et al. α11β1 Integrin is Induced in a Subset of Cancer-Associated Fibroblasts in Desmoplastic Tumor Stroma and Mediates In Vitro Cell Migration. Cancers (Basel). 2019;11(6).

18. Kürten CHL, Kulkarni A, Cillo AR, Santos PM, Roble AK, Onkar S, et al. Investigating immune and non-immune cell interactions in head and neck tumors by single-cell RNA sequencing. Nature Communications. 2021;12(1):7338.

19. Tremble LF, McCabe M, Walker SP, McCarthy S, Tynan RF, Beecher S, et al. Differential association of CD68+ and CD163+ macrophages with macrophage enzymes, whole tumour gene expression and overall survival in advanced melanoma. British Journal of Cancer. 2020;123(10):1553-61.

20. Deeb G, Wang J, Ramnath N, Slocum HK, Wiseman S, Beck A, et al. Altered E-cadherin and epidermal growth factor receptor expressions are associated with patient survival in lung cancer: a study utilizing high-density tissue microarray and immunohistochemistry. Modern Pathology. 2004;17(4):430-9.

21. Gieniec KA, Butler LM, Worthley DL, Woods SL. Cancer-associated fibroblasts—heroes or villains? British Journal of Cancer. 2019;121(4):293-302.

22. Liu T, Han C, Wang S, Fang P, Ma Z, Xu L, et al. Cancer-associated fibroblasts: an emerging target of anti-cancer immunotherapy. Journal of Hematology & Oncology. 2019;12(1):86.

23. Berg S, Kutra D, Kroeger T, Straehle CN, Kausler BX, Haubold C, et al. ilastik: interactive machine learning for (bio)image analysis. Nature Methods. 2019;16(12):1226-32.

24. Stirling DR, Carpenter AE, Cimini BA. CellProfiler Analyst 3.0: accessible data exploration and machine learning for image analysis. Bioinformatics. 2021;37(21):3992-4.

25. Vito RT Zanotelli BB. ImcSegmentationPipeline: A pixelclassification based multiplexed image segmentation pipeline. Zenodo. 2017.

26. Schapiro D, Jackson HW, Raghuraman S, Fischer JR, Zanotelli VRT, Schulz D, et al. histoCAT: analysis of cell phenotypes and interactions in multiplex image cytometry data. Nature Methods. 2017;14(9):873-6.

27. Jackson HW, Fischer JR, Zanotelli VRT, Ali HR, Mechera R, Soysal SD, et al. The single-cell pathology landscape of breast cancer. Nature. 2020;578(7796):615-20.

28. Keren L, Bosse M, Marquez D, Angoshtari R, Jain S, Varma S, et al. A Structured Tumor-Immune Microenvironment in Triple Negative Breast Cancer Revealed by Multiplexed Ion Beam Imaging. Cell. 2018;174(6):1373-87.e19.

29. Van Gassen S, Callebaut B, Van Helden MJ, Lambrecht BN, Demeester P, Dhaene T, et al. FlowSOM: Using self-organizing maps for visualization and interpretation of cytometry data. Cytometry Part A. 2015;87(7):636-45.

30. Wilkerson MD, Hayes DN. ConsensusClusterPlus: a class discovery tool with confidence assessments and item tracking. Bioinformatics. 2010;26(12):1572-3.

31. enbabaoğlu Y, Michailidis G, Li JZ. Critical limitations of consensus clustering in class discovery. Scientific Reports. 2014;4(1):6207.

32. Levine JH, Simonds EF, Bendall SC, Davis KL, Amir E-aD, Tadmor MD, et al. Data-Driven Phenotypic Dissection of AML Reveals Progenitor-like Cells that Correlate with Prognosis. Cell. 2015;162(1):184-97.

33. Stanley N, Stelzer IA, Tsai AS, Fallahzadeh R, Ganio E, Becker M, et al. VoPo leverages cellular heterogeneity for predictive modeling of single-cell data. Nature Communications. 2020;11(1):3738.

34. Lee H-C, Kosoy R, Becker CE, Dudley JT, Kidd BA. Automated cell type discovery and classification through knowledge transfer. Bioinformatics (Oxford, England). 2017;33(11):1689-95.

35. van der Maaten L, Hinton G. Visualizing Data using t-SNE. Journal of Machine Learning Research. 2008;9:2579-605.

36. Eling N, Damond N, Hoch T, Bodenmiller B. cytomapper: an R/Bioconductor package for visualization of highly multiplexed imaging data. Bioinformatics. 2020;36(24):5706-8.

37. Somarakis A, Unen VV, Koning F, Lelieveldt B, Höllt T. ImaCytE: Visual Exploration of Cellular Micro-Environments for Imaging Mass Cytometry Data. IEEE Transactions on Visualization and Computer Graphics. 2021;27(1):98-110.

38. Costa A, Kieffer Y, Scholer-Dahirel A, Pelon F, Bourachot B, Cardon M, et al. Fibroblast Heterogeneity and Immunosuppressive Environment in Human Breast Cancer. Cancer Cell. 2018;33(3):463-79.e10.

39. Bhattacharjee S, Hamberger F, Ravichandra A, Miller M, Nair A, Affo S, et al. Tumor restriction by type I collagen opposes tumor-promoting effects of cancer-associated fibroblasts. The Journal of Clinical Investigation. 2021;131(11).

40. Sukswai N, Khoury JD. Immunohistochemistry Innovations for Diagnosis and Tissue-Based Biomarker Detection. Curr Hematol Malig Rep. 2019;14(5):368-75.

41. Matos LLd, Trufelli DC, de Matos MGL, da Silva Pinhal MA. Immunohistochemistry as an important tool in biomarkers detection and clinical practice. Biomark Insights. 2010;5:9-20.

42. Schlecht A, Boneva S, Salie H, Killmer S, Wolf J, Hajdu RI, et al. Imaging mass cytometry for high-dimensional tissue profiling in the eye. BMC Ophthalmol. 2021;21(1):338-.

43. Bandura DR, Baranov VI, Ornatsky OI, Antonov A, Kinach R, Lou X, et al. Mass Cytometry: Technique for Real Time Single Cell Multitarget Immunoassay Based on Inductively Coupled Plasma Time-of-Flight Mass Spectrometry. Analytical Chemistry. 2009;81(16):6813-22.

44. Giesen C, Wang HAO, Schapiro D, Zivanovic N, Jacobs A, Hattendorf B, et al. Highly multiplexed imaging of tumor tissues with subcellular resolution by mass cytometry. Nature Methods. 2014;11(4):417-22.

45. Kuett L, Catena R, Özcan A, Plüss A, Ali HR, Sa'd MA, et al. Three-dimensional imaging mass cytometry for highly multiplexed molecular and cellular mapping of tissues and the tumor microenvironment. Nature Cancer. 2022;3(1):122-33.

46. Danenberg E, Bardwell H, Zanotelli VRT, Provenzano E, Chin S-F, Rueda OM, et al. Breast tumor microenvironment structures are associated with genomic features and clinical outcome. Nature Genetics. 2022.

47. Kakade VR, Weiss M, Cantley LG. Using Imaging Mass Cytometry to Define Cell Identities and Interactions in Human Tissues. Frontiers in Physiology. 2021;12.

48. Windhager J, Bodenmiller B, Eling N. An end-to-end workflow for multiplexed image processing and analysis. bioRxiv. 2021:2021.11.12.468357.

49. Obradovic A, Graves D, Korrer M, Wang Y, Roy S, Naveed A, et al. Immunostimulatory cancer-associated fibroblast subpopulations can predict immunotherapy response in head and neck cancer. Clin Cancer Res. 2022.

50. D'Arcangelo E, Wu NC, Cadavid JL, McGuigan AP. The life cycle of cancer-associated fibroblasts within the tumour stroma and its importance in disease outcome. British Journal of Cancer. 2020;122(7):931-42.

Figure legends

Figure 1. Visualization of structural, stromal, and vascular components of tumor by imaging mass cytometry and immunohistochemistry in an oral squamous cell carcinoma cTMA core. E-cadherin (red) staining the tumor epithelial compartment, collagen-1 (green) and tenascin-C (blue) staining the stroma and CD31 (cyan) and podoplanin (magenta) staining the blood vessels and lymph vessels, respectively. Scale bar- 100 μm for IMC and IHC images.

Figure 2. Detection of different CAF markers in osteosarcoma cTMA core by imaging mass cytometry and immunohistochemistry. CAFs expressing α-SMA (blue), FAP (white), integrin α11 (red) and collagen-1 (green) could be detected. Scale bar- 100 μm for IMC and IHC images. α-SMA: alpha-smooth muscle actin, FAP: fibroblast activation protein.

Figure 3. Simultaneous visualization of various immune cell subsets in a tonsil cTMA core: T-helper cells (green, $CD4^+$), cytotoxic T-cells (white, $CD8^+$), regulatory T-cells ($CD4^+$, $FoxP3^+$, red), B-cells (blue, $CD20^+$) and macrophages (magenta, $CD68^+$). Scale bar- 100 μm for IMC and IHC images. FoxP3: forkhead box P3.

Figure 4. Single-cell clustering using in-house informatics pipeline. A) Distribution of cells according to tissue type visualized after dimensionality reduction using t-SNE. B) Distribution of cells based on marker expression and phenotype in the same t-SNE. C and D) Number of cells and relative percentage in each cluster related to tissue type. E) Heatmap depicting nine different clusters based on unsupervised clustering. Six major CAF cluster after negative selection (E-cadherin-, CD4- and CD31-) could be identified. T-SNE: t-distributed Stochastic Neighbor Embedding. OSCC: oral squamous cell carcinoma. FSP-1: fibroblast specific protein-1, α-SMA: alpha-smooth muscle actin, FAP: fibroblast activation protein.

Figure 5. Visual comparison of cells in tissues between in-house informatics pipeline and ImaCytE. A) Visualization of CAF phenotypes in various tissues using in-house informatics pipeline. The clusters used is the same as that represented earlier. B) Visualization of cells in tissues using ImaCytE. C) Heatmap of various cell clusters based on unsupervised clustering obtained from intuitive software, ImaCytE. CAF phenotypes of interest are indicated with number of cells in clusters beneath indication color. OSCC: oral squamous cell carcinoma. FSP-1: fibroblast specific protein-1, α-SMA: alpha-smooth muscle actin, FAP: fibroblast activation protein.

Supplementary Figure S1. Comparison between staining obtained by imaging mass cytometry and immunohistochemistry of NG-2, VE-cadherin, granzyme B and PD-L1 markers in oral squamous cell carcinoma and placenta cTMA. Full forms of NG-2, VE-cadherin and PD-L1.

Supplementary Figure S2. Visualization of different markers in the oral squamous cell carcinoma cTMA using IMC and IHC. EGFR (cyan) staining the tumor epithelia, Ki-67 (red) staining the proliferating cells both in the tumor epithelia and stroma, CD31 (yellow), VEGFR-2 (magenta) and podoplanin (blue) staining the blood vessels and lymph vessels, respectively. Scale bar- 100 µm for IMC and IHC images.

Supplementary Figure S3. Additional CAF markers in osteosarcoma cTMA. FSP-1 (red), CD140β (blue), CD90 (yellow), caveolin-1 (green) and YAP-1 (magenta) can be successfully visualized in the tissue section. Scale bar- 100 µm for IMC and IHC images. FSP-1: fibroblast specific protein-1, YAP-1: yes-associated protein-1.

Supplementary Figure S4. Visualization of various immune subsets in the oral squamous cell carcinoma cTMA. Natural killer (NK) cells (yellow) and tumor infiltrating cytotoxic T-cell (CD8+, red) can be observed in the tumor epithelia, whereas majority of T-regulatory cells (CD4+, blue), B-cell (CD20+ cyan) and M2-like macrophages (CD163+, green) can be observed in the tumor stroma. Scale bar- 100 um for IMC images and 20x magnification and scale bar- 100 µm for IHC images.

Supplementary Figure S5. Cell segmentation and annotation of single-cells using the in-house bioinformatics pipeline. A) t-SNE plot showing the identified phenotypes across the studied tissue. B) Bar plot showing the number of segmented cells per tissue. C) Scatter plot showing the PAC score for different metaclusters identified by the ConsensusClustering approach. Vertical and horizontal red lines indicate the cut-off of 1 % PAC used to merge clusters with known phenotypic profiles. D) Bar plot showing the total number of cells in each of the studied cell types. The color code matches the t-SNE plot presented in subplot (A).

Supplementary Figure S6. Visualization of single-cells using t-SNE. Each subplot is colored based on the z-scored intensity values of different AB channels available in our AB panel.

Table 1. Overview of all markers used in study, metal tags used with each AB, concentration, and incubation step.

Supplementary Table 1. Overview of tissue types (control tissue micro array) used in study.

1 Data Availability Statement

The datasets for this study are publicly available at https://github.com/StiThor/Development-of-antibody-panel-for-imaging-mass-cytometry-to-investigate-cancer-associated-fibroblast .

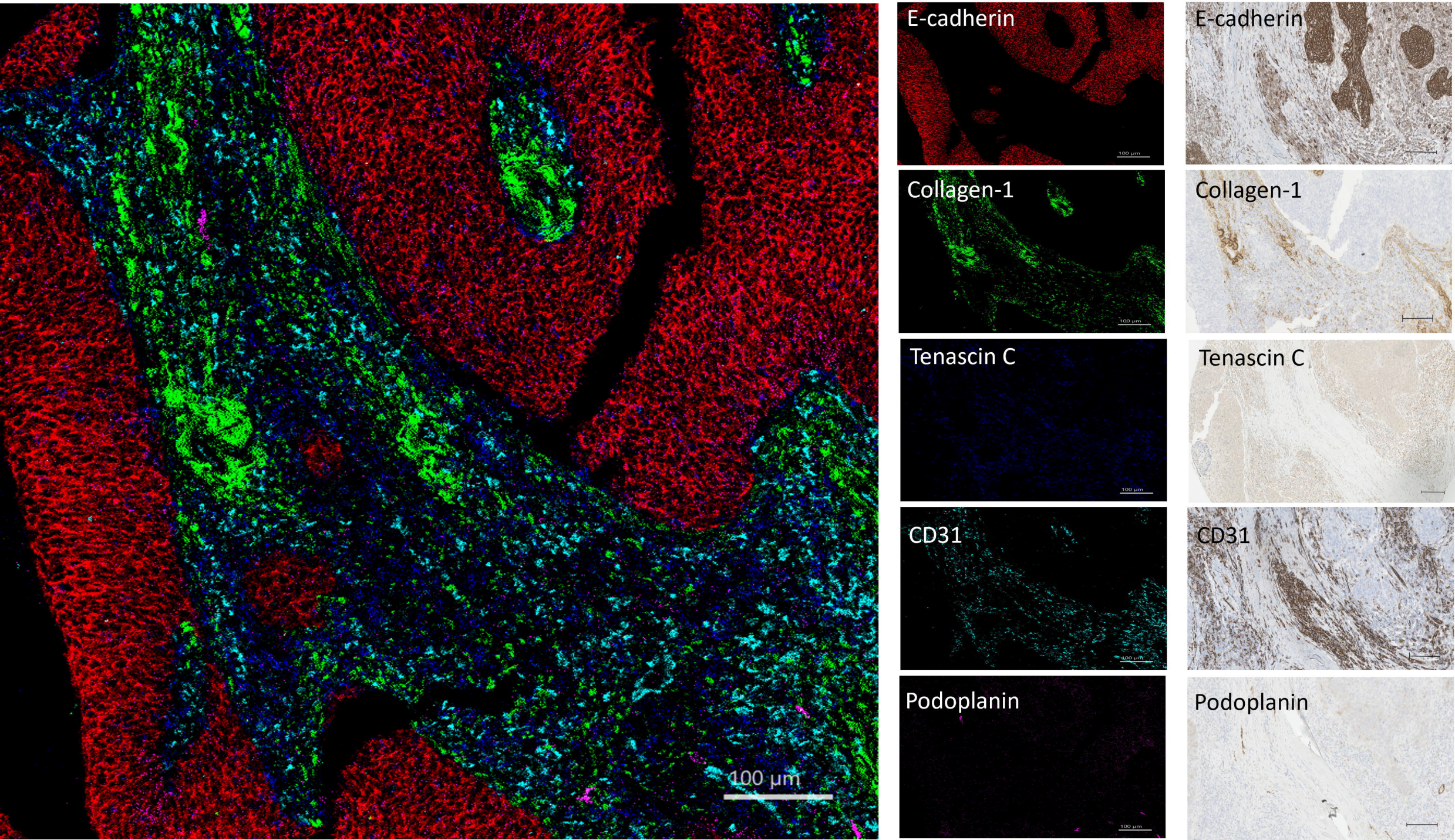
100 µm
E-cadherin
Collagen-1
Tenascin C
CD31
Podoplanin
E-cadherin
Collagen-1
Tenascin C
CD31
Podoplanin

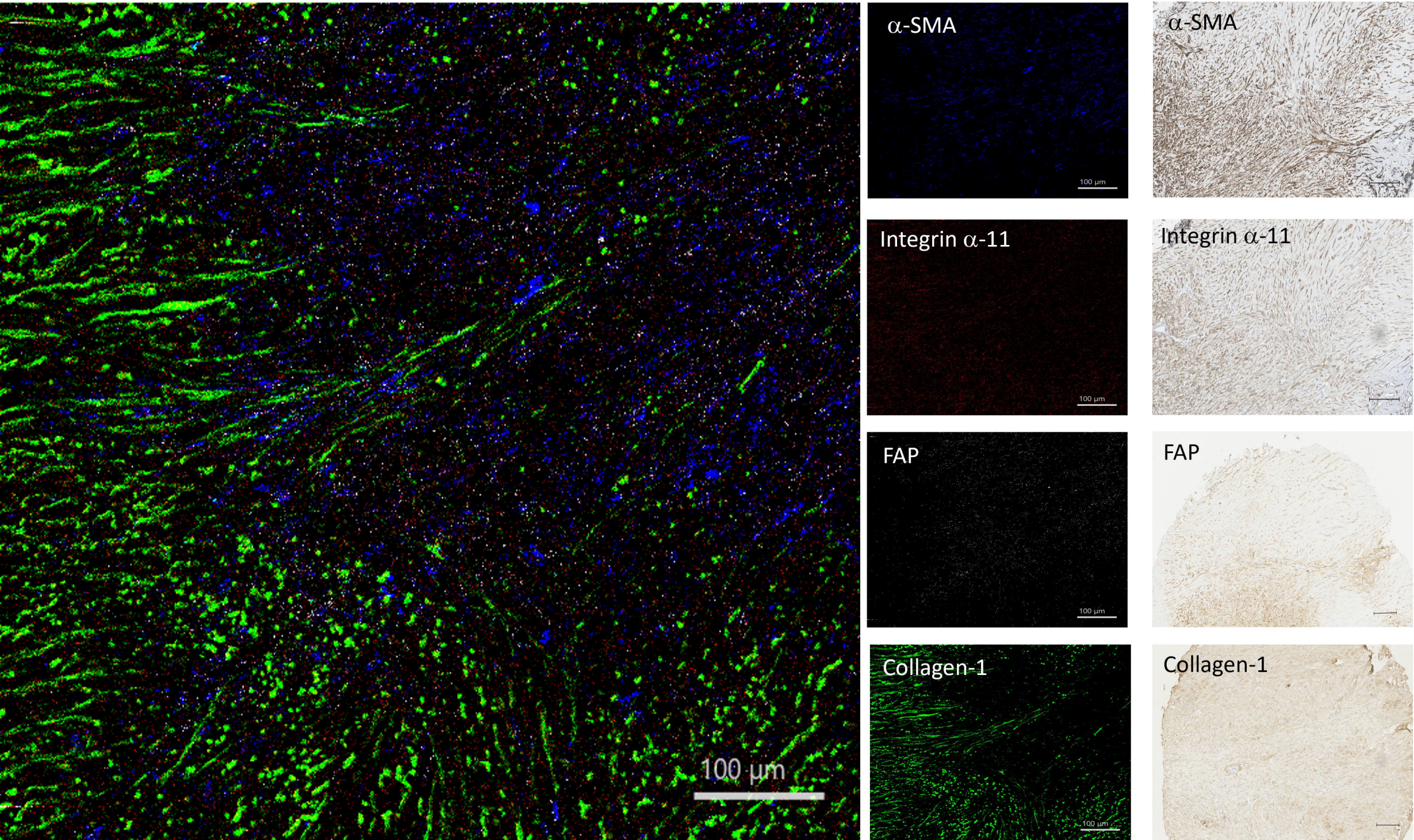
100 µm
α-SMA
100 µm
α-SMA
Integrin α-11
100 µm
Integrin α-11
FAP
100 µm
FAP
Collagen-1
100 µm
Collagen-1

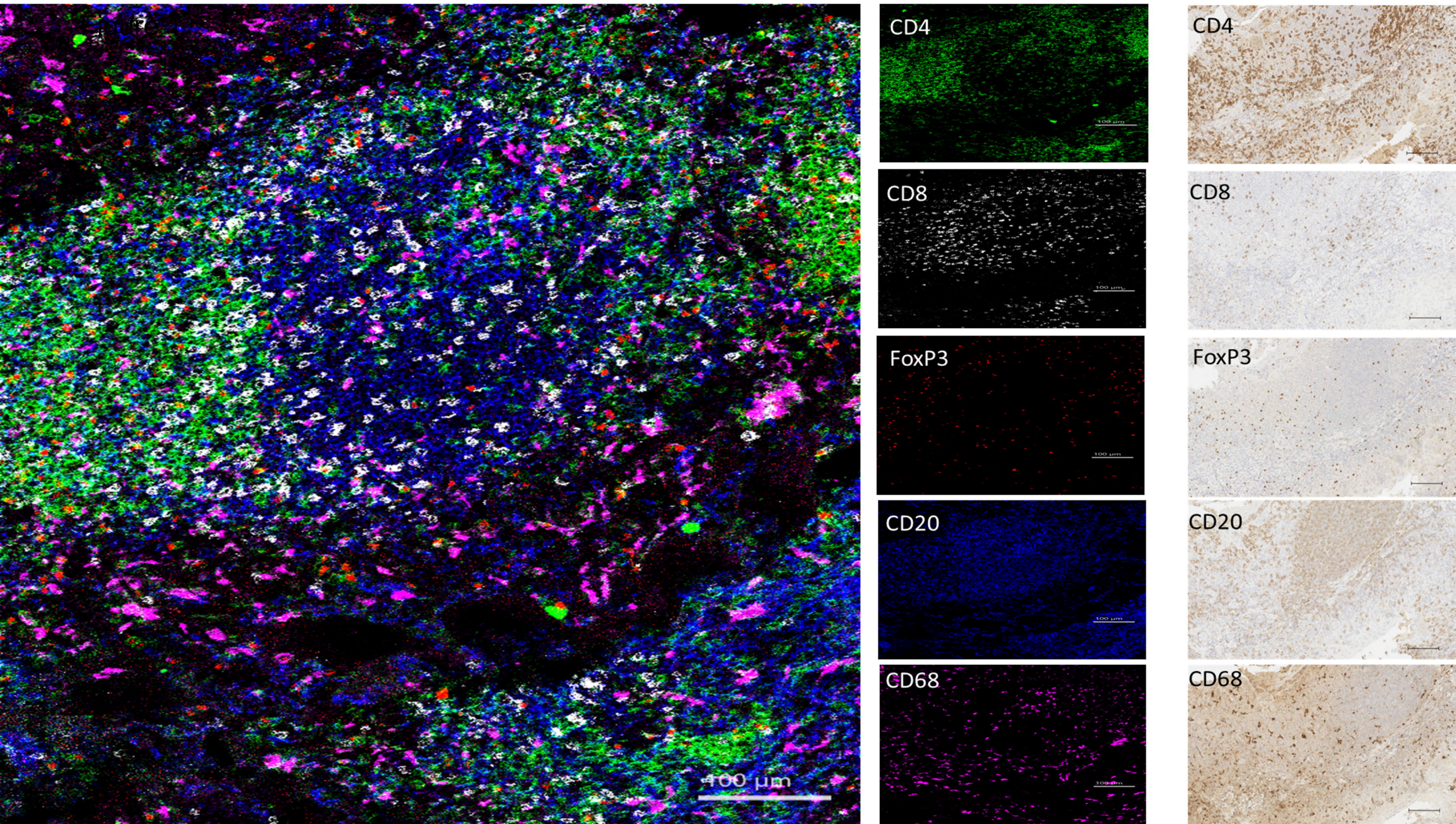
100 µm
CD4
CD8
FoxP3
CD20
CD68
CD4
CD8
FoxP3
CD20
CD68

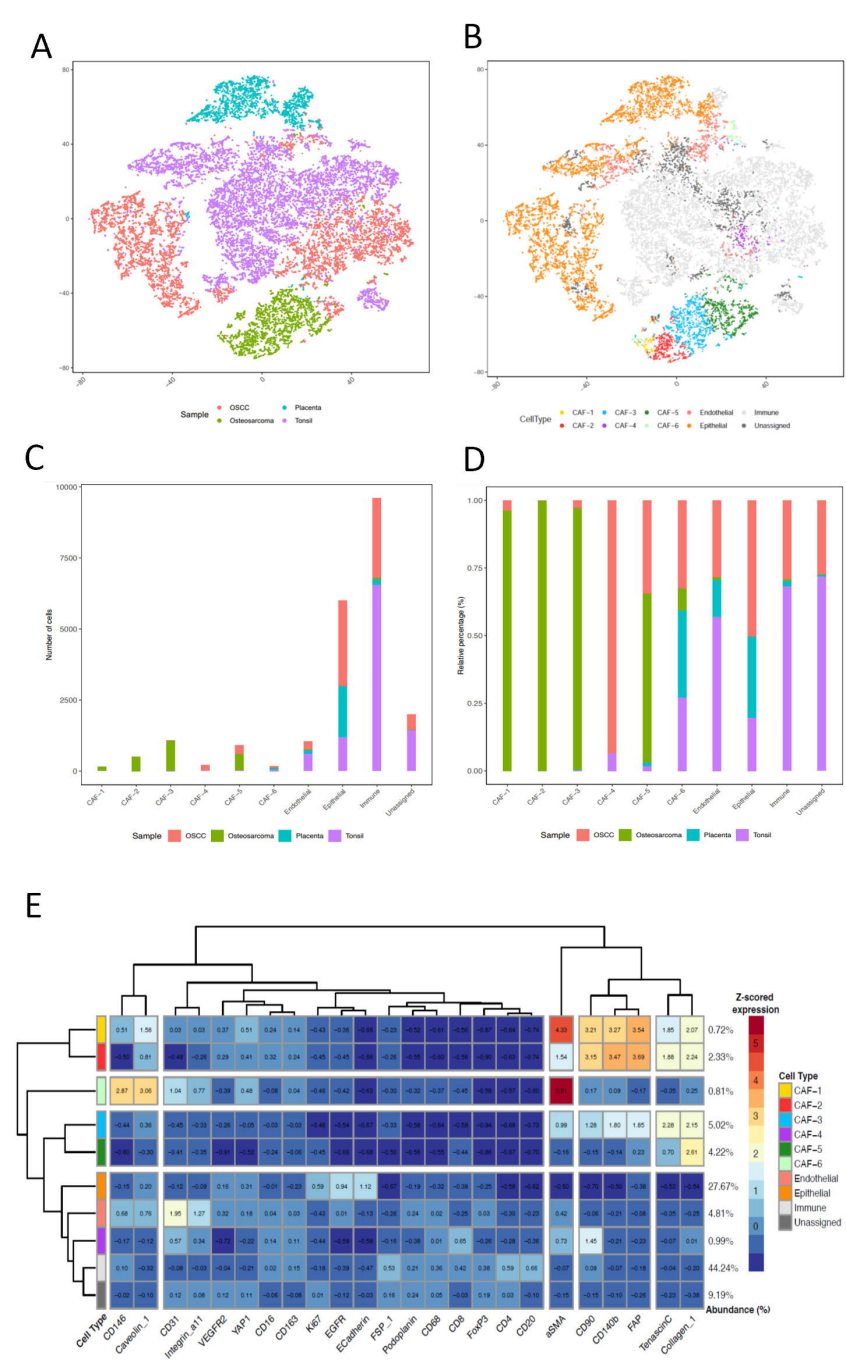
A
Sample
OSCC
Osteosarcoma
Placenta
Tonsil
B
CellType
CAF−1
CAF−2
CAF−3
CAF−4
CAF−5
CAF−6
Endothelial
Epithelial
Immune
Unassigned
C
Number of cells
Sample
OSCC
Osteosarcoma
Placenta
Tonsil
D
Relative percentage (%)
Sample
OSCC
Osteosarcoma
Placenta
Tonsil
E
Z-scored expression
Cell Type
CAF−1
CAF−2
CAF−3
CAF−4
CAF−5
CAF−6
Endothelial
Epithelial
Immune
Unassigned
Abundance (%)
0.72%
2.33%
0.81%
5.02%
4.22%
27.67%
4.81%
0.99%
44.24%
9.19%
Cell Type
CD146
Caveolin_1
CD31
Integrin_a11
VEGFR2
YAP1
CD16
CD163
Ki67
EGFR
ECadherin
FSP_1
Podoplanin
CD68
CD8
FoxP3
CD4
CD20
aSMA
CD90
CD140b
FAP
TenascinC
Collagen_1

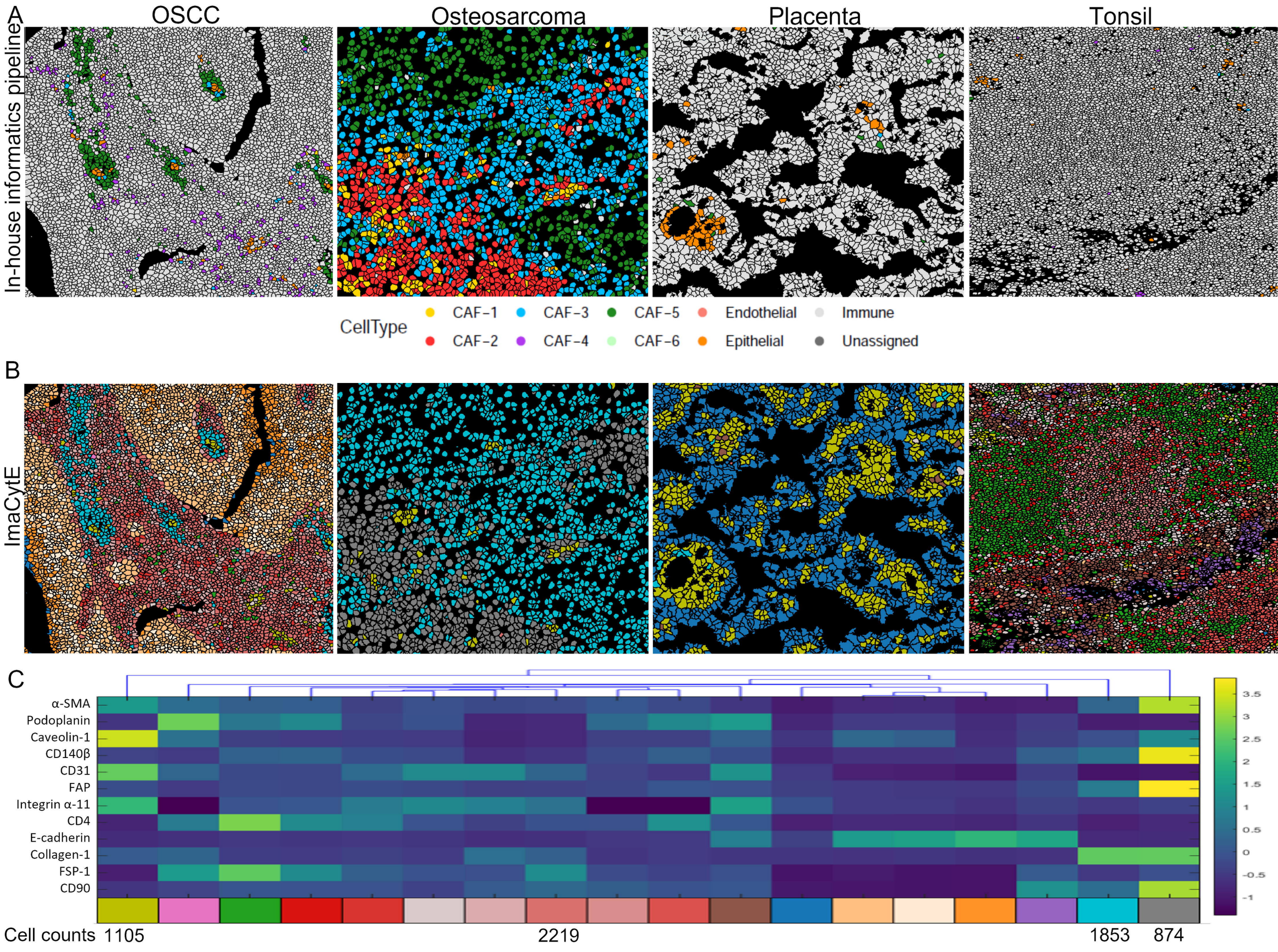
A
OSCC
Osteosarcoma
Placenta
Tonsil
In-house informatics pipeline
CellType
CAF−1
CAF−2
CAF−3
CAF−4
CAF−5
CAF−6
Endothelial
Epithelial
Immune
Unassigned
B
ImaCytE
C
α-SMA
Podoplanin
Caveolin-1
CD140β
CD31
FAP
Integrin α-11
CD4
E-cadherin
Collagen-1
FSP-1
CD90
3.5
3
2.5
2
1.5
1
0.5
0
-0.5
-1
Cell counts 1105
2219
1853
874

						Incubation	
Marker	**Suppliers**	**Clone**	**Metal**	**In-house conjugation**	**Concentration**	**Overnight 4°c**	**RT (1 hr)**
α-SMA	Fluidigm	1A4	141 Pr	No	1:400	x	
α–11	UiB	Clone 24	153 Eu	Yes	1:1000	x	
FAP	CST	E1V9V	152 Sm	Yes	1:1000	x	
FSP-1/S100A4	CST	D9F9D	172 Yb	Yes	1:2000	x	
CD140β	CST	28E1	149 Sm	Yes	1:200	x	
CD90/Thy-1	CST	D3V8A	176 Yb	Yes	1:1000	x	
Ki-67	Fluidigm	B56	168 Er	No	1:200	x	
Caveolin	CST	D46G3	145 Nd	Yes	1:2000		x
CD16	Fluidigm	EPR16784	146 Nd	No	1:50		x
CD68	Fluidigm	KP1	159 Tb	No	1:50	x	
CD163	Fluidigm	EDHu-1	147 Sm	No	1:600	x	
CD4	Fluidigm	EPR6855	156 Gd	No	1:200	x	
CD8a	Fluidigm	CD8/144B	162 Dy	No	1:100	x	
CD20	Fluidigm	H1	161 Dy	No	1:400	x	
FoxP3	Fluidigm	236A/E7	155 Gd	No	1:50	x	
CD31	Fluidigm	EPR3094	151 Eu	No	1:100	x	
VEGFR2	CST	D5B1	165 Ho	Yes	1:3000	x	
Podoplanin	CST	LpMab-12	143 Nd	Yes	1:500	x	
CD146	Abcam	EPR3208	175 Lu	Yes	1:2000	x	
Collagen type 1	Fluidigm	Polyclonal	169 Tm	No	1:600	x	
Tenascin C	Merck	BC-24	163 Dy	Yes	1:1000	x	
E-cadherin	Fluidigm	24E10	158 Gd	No	1:100	x	
EGFR	Fluidigm	D38B1	142 Nd	No	1:100	x	
YAP-1	CST	D8H1X	144 Nd	Yes	1:3000	x	
Granzyme B	Fluidigm	EPR20129-217	167 Er	No	1:100	-	-
VE-cadherin	CST	E6N7A	148 Nd	Yes	1:25	-	-
NG-2	CST	E3B3G	160 Gd	Yes	1:1000	-	-
PD-L1	Fluidigm	SP142	150 Nd	No	1:50	-	-
VEGFR3	CST	C82A2 and C28G5	-	Not conjugated	1:50 - 1:1000	-	-
pTAK	CST	90C7	-	Not conjugated	1:50 - 1:1000	-	-
pFAK	CST	D20B1	-	Not conjugated	1:50 - 1:1000	-	-
BNIP3	CST	D7U1T	-	Not conjugated	1:50 - 1:1000	-	-
NRP2	AH diagnostics	C-9	-	Not conjugated	1:50 - 1:1000	-	-